

Separating the BL Lac and Cluster X-ray Emissions in Abell 689 with *Chandra*

P. A. Giles*, B. J. Maughan, M. Birkinshaw, D. M. Worrall, K. Lancaster

HH Wills Physics Laboratory, Tyndall Avenue, Bristol, BS8 1TL, UK

Accepted 2011 August 26. Received 2011 August 4; in original form 2011 March 10

ABSTRACT

We present the results of a *Chandra* observation of the galaxy cluster Abell 689 ($z=0.279$). Abell 689 is one of the most luminous clusters detected in the ROSAT All Sky Survey (RASS), but was flagged as possibly including significant point source contamination. The small PSF of the *Chandra* telescope allows us to confirm this and separate the point source from the extended cluster X-ray emission. For the cluster we determine a bolometric luminosity of $L_{\text{bol}} = (3.3 \pm 0.3) \times 10^{44} \text{ erg s}^{-1}$ and a temperature of $kT = 5.1^{+2.2}_{-1.3} \text{ keV}$ when including a physically motivated background model. We compare our measured luminosity for A689 to that quoted in the Rosat All Sky Survey (RASS) and find $L_{0.1-2.4, \text{keV}} = 2.8 \times 10^{44} \text{ erg s}^{-1}$, a value ~ 10 times lower than the ROSAT measurement. Our analysis of the point source shows evidence for significant pileup, with a pile-up fraction of $\simeq 60\%$. SDSS spectra and HST images lead us to the conclusion that the point source within Abell 689 is a BL Lac object. Using radio and optical observations from the VLA and HST archives, we determine $\alpha_{\text{ro}}=0.50$, $\alpha_{\text{ox}}=0.77$ and $\alpha_{\text{rx}}=0.58$ for the BL Lac, which would classify it as being of ‘High-energy peak BL Lac’ (HBL) type. Spectra extracted of A689 show a hard X-ray excess at energies above 6 keV that we interpret as inverse Compton emission from aged electrons that may have been transported into the cluster from the BL Lac.

Key words: galaxies: clusters: general – galaxies: clusters: individual: Abell 689 – BL Lacertae objects: general

1 INTRODUCTION

Studies of clusters of galaxies, including measurements of their number density and growth from the highest density perturbations in the early Universe, offer insight into the underlying cosmology (Vikhlinin et al. 2003; Allen et al. 2004). However, in order to use clusters as a cosmological probe three essential tools are required (Del Popolo et al. 2010): (a) an efficient method to find clusters over a wide redshift range, (b) an observational method of determining the cluster mass, and (c) a method to compute the selection function or the survey volume in which clusters are found. These requirements are met by large surveys with well understood selection criteria. Arguably the most effective method of building large, well defined cluster samples has been via X-ray selection. The high X-ray luminosities of clusters make it relatively easy to detect and study clusters out to high redshifts.

Many cluster samples have been constructed based

upon large X-ray surveys such as the Einstein Medium Sensitivity Survey (EMSS; Gioia et al. 1990) and the ROSAT All Sky Survey (RASS; Voges 1992). However due to the relatively poor angular resolution of these X-ray observatories, observations of clusters were susceptible to point source contamination. Indeed, within the ROSAT Brightest Cluster Sample (BCS; Ebeling et al. 1998) and its low-flux extension (eBCS; Ebeling et al. 2000), 9 out of 201 clusters and 8 out of 99 clusters respectively were flagged as probably having a significant fraction of the quoted flux from embedded point sources. Being able to resolve these point sources is of crucial importance for the reliable estimation of cluster properties, and indeed the nature of the point source contamination is of independent interest.

The study of galaxy clusters has been transformed with the launch of powerful X-ray telescopes such as *Chandra* and XMM Newton, which have allowed the study of the X-ray emitting intracluster medium (ICM) with unprecedented detail and accuracy. With the launch of this new generation of X-ray telescopes, we are able to uncover interesting features in the morphologies of individual clusters. In particu-

* E-mail: P.Giles@bristol.ac.uk

lar, *Chandra*'s high angular resolution provides the means to examine individual cluster features with great detail.

Abell 689 (hereafter A689; Abell 1958), at $z=0.279$ (Collins et al. 1995), was detected in the RASS in an accumulated exposure time of 317s. It is included in the BCS, with a measured X-ray luminosity of 3.0×10^{45} erg s^{-1} in the 0.1–2.4 keV band. This luminosity is the third highest in the BCS, and thus A689 meets the selection criteria for various highly X-ray luminous cluster samples (e.g. Dahle et al. 2002). However this cluster was noted as having possible point source contamination, and for this reason has often been rejected from many flux limited samples. In this study we present results of *Chandra* observations designed to separate any point sources and determine uncontaminated cluster properties.

The outline of this paper is as follows. In § 2 we discuss the observation and data analysis. Results of the X-ray cluster analysis is presented in § 3. In § 4 we present our analysis of the X-ray point source through X-ray, optical and radio observations. We interpret our results in § 5 and the conclusions are presented in § 6. Throughout this paper we adopt a cosmology with $\Omega_M = 0.3$, $\Omega_\Lambda = 0.7$ and $H_0 = 70$ km s^{-1} Mpc $^{-1}$, so that 1'' corresponds to 4.22 kpc at the redshift of A689. We define spectral index, α , in the sense $S \propto \nu^{-\alpha}$.

2 OBSERVATIONS AND DATA REDUCTION

The *Chandra* observation of A689 (ObsID 10415) was carried out January 01, 2009. A summary of the cluster's properties is presented in Table 1. The observation was taken in VFaint mode, and the source was observed in an ACIS-I configuration at the aim point of the I3 chip, with the ACIS S2 chip also turned on.

For the imaging analysis of the cluster we used the CIAO¹ 4.2 software package with CALDB² version 4.3.0 and followed standard reduction methods. Since our observation was telemetered in VFaint mode additional background screening was applied by removing events with significantly positive pixels at the border of the 5×5 event island³. We inspected background light curves of the observation following the recommendations given in Markevitch et al. (2003), to search for possible background fluctuations. The light curve was cleaned by 3σ clipping and periods with count rates $>20\%$ above the mean rate were rejected. curve with rejected periods showed in red. The final level-2 event file had a total cleaned exposure time of 13.862 ks.

As discussed in Sect. 4, there is a bright point source at the center of the extended cluster emission which is affected by pileup. For the analysis of this source we followed the same reduction method, with the exception that VFaint cleaning was not applied. Applying VFaint cleaning leads to incorrect rejection of piled-up events, introducing artifacts in the data.

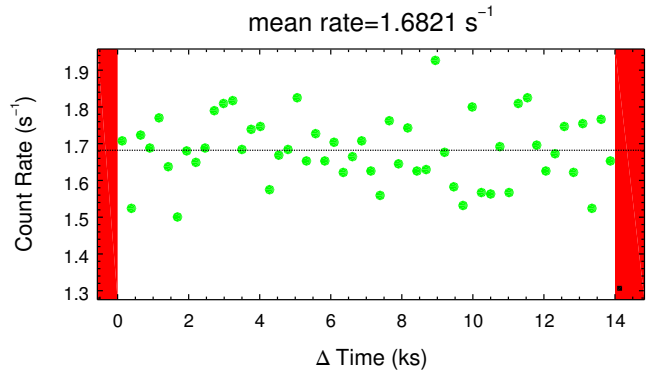


Figure 1. Background light curve for the observation of A689 in the 0.3–12.0 keV band. The CCD on which the cluster falls (ACIS-I3) and all point sources are excluded. The red bands show periods excluded by the Good Time Interval (GTI) file.

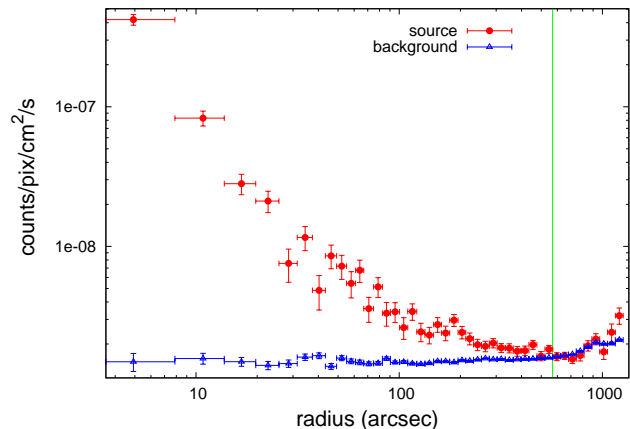


Figure 3. Exposure-corrected radial surface brightness profiles (0.7–2.0 keV band) of the cluster (red) and the blank-sky background (blue), with the green line representing the radius beyond which no significant cluster emission is detected.

3 X-RAY CLUSTER ANALYSIS

In this section we determine global cluster properties of Abell 689. Figure 2 shows a Gaussian smoothed image of the cleaned level 2 events file in the 0.7–2.0 keV band (the readout streak is removed using the CIAO tool ACISREAD-CORR), with an inset image of the point source which lies at the center of the cluster. The extent of the diffuse cluster emission was determined by plotting an exposure-corrected radial surface brightness profile (Fig 3), in the 0.7–2.0 keV band, of both the observation and blank-sky background to determine where the cluster emission is lost against the background. Figure 3 demonstrates that the diffuse cluster emission is detectable to a radius $r \approx 570''$ (≈ 2.41 Mpc). At large radii ($r \geq 700''$) the curves rise due to vignetting corrections (larger at larger radii) applied to all the counts, whereas in reality each curve contains a component from particles that have not been focused by the telescope.

¹ See <http://cxc.harvard.edu/ciao/>

² See <http://cxc.harvard.edu/caldb/>

³ See <http://cxc.harvard.edu/ciao/why/aciscleanvf.html>

Name	RA	Dec	z	$N_{\text{H,Gal}}$	RASS $L_{\text{X},0.1-2.4\text{keV}}$
Abell 689	08 ^h 37 ^m 24 ^s .70	+14° 58' 20".78	0.279	$3.66 \times 10^{20} \text{ cm}^{-2}$	$30.4 \times 10^{44} \text{ erg s}^{-1}$

Table 1. Basic properties. Columns: (1) = Source name; (2) = Right Ascension at J2000 from *Chandra*; (3) = Declination at J2000 from *Chandra*; (4) = Redshift; (5) = Galactic column density; (6) = Intrinsic X-ray luminosity in the 0.1–2.4 keV band based upon ROSAT observations (Ebeling et al. 1998).

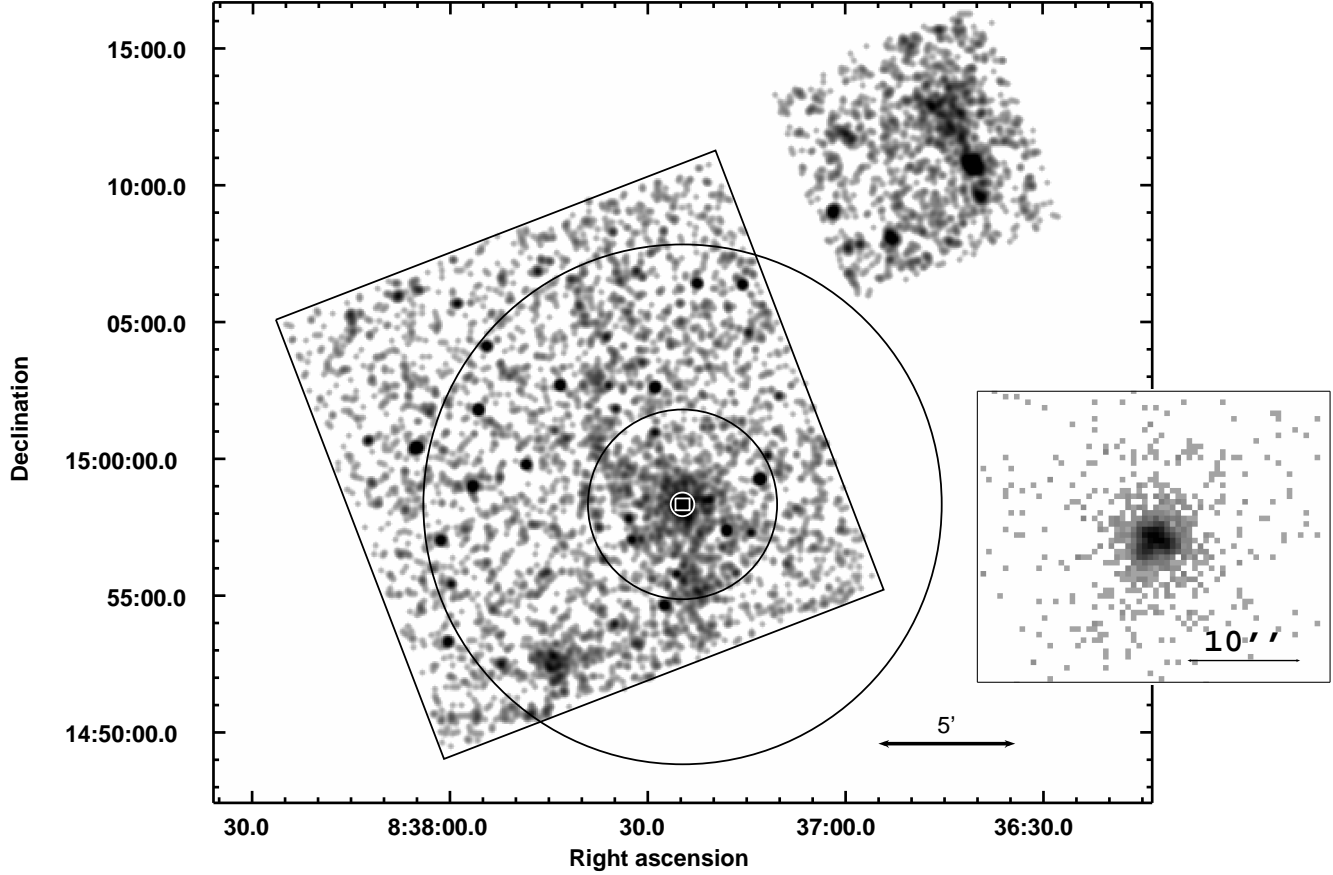


Figure 2. 0.7–2.0 keV image of A689, smoothed by a Gaussian ($\sigma=1.5$ pixels, where 1 pixel = $3.94''$), cleaned in VFAINT mode and with the readout streak removed. Inset is a zoomed-in unbinned image of the central point source within A689, cleaned in FAINT mode (see § 2). The inner black circle ($r = 208''$) is the region in which we extract the spectra for our analysis of the cluster emission (see § 3.2), the outer black circle ($r = 570''$) represents the detected cluster radius (see § 3), and the region between this and the black box was used for the local background (see § 3.2). The white box displays the size of the inset, and the inner white circle ($r = 26''$) shows the region excluded due to the central point source. Many point sources are seen in the observation and are excluded from our analysis. An extended source on the NE chip can be seen, that is unrelated to A689 and is also excluded from our analysis.

3.1 Background Subtraction

In order to take the background of the observation into account, appropriate period E *Chandra* blank-sky backgrounds were obtained, processed identically to the cluster, and reprojected onto the sky to match the cluster observation. We then followed a method similar to that outlined in Vikhlinin et al. (2006), in order to improve the accuracy of the background by applying small adjustments to the baseline model. Firstly we corrected for the rate of charged particle events, which has a secular and short-term variation by as much as 30%. We renormalise the background in the 9.5–12 keV band, where the *Chandra* effective area is nearly zero and the observed flux is due entirely to the particle

background events. The renormalisation factor was derived by taking the ratio of the observed count rate in the source and background observations respectively. The normalised spectrum of the blank-sky background is shown in Figure 4, over-plotted on the local background for comparison. The spectra agree well in the 9.5–12.0 keV band, and across the whole spectrum with only slight differences. In addition to the particle background, the blank-sky and source observations contain differing contributions from the soft X-ray background, containing a mixture of the Galactic and geocoronal backgrounds, significant at energies ≤ 1 keV. To take into account any difference in this background component between the blank-sky and source observations, the spectra were subtracted and residuals were modeled in the 0.4–1 keV

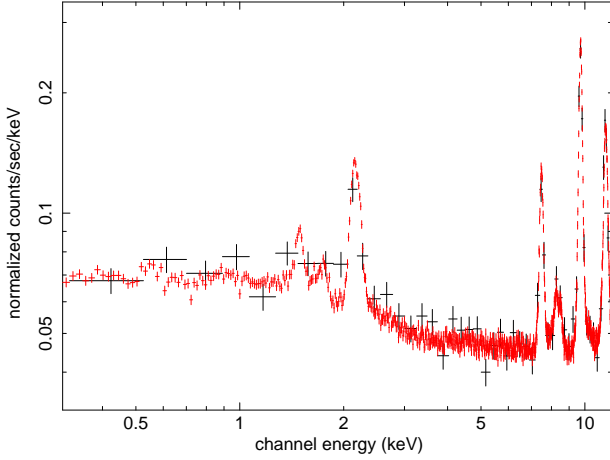


Figure 4. Comparison of the local (black) and blank-sky (red) background spectra, normalised to match in the 9.5–12.0 keV band.

band using an APEC thermal plasma model (Smith et al. 2001). This model was included in the spectral fitting for the cluster analysis. As can be seen in Figure 4 this component is very weak in the case of A689.

3.2 X-ray Cluster Properties

The analysis of the diffuse X-ray emission allows us to determine the X-ray environment surrounding the cluster central point source. Throughout this process we excluded the central point source (Fig 2; $r \leq 26''$) and the associated readout streaks to avoid contaminating the cluster emission.

To determine cluster properties we extract spectra out to a radius chosen so that the cluster has the maximum possible signal-to-noise (SNR). The net number of counts, corrected for background, is then 414 (with $\text{SNR} = 15$) and the extraction annulus is $26'' < r < 208''$ (see Fig 2), centered on the cluster (at $\alpha, \delta = 08^{\text{h}} 37^{\text{m}} 24^{\text{s}}.70, 14^{\circ} 58' 20''.78$). We fitted the extracted spectrum in *XSPEC* with an absorbed thermal plasma model (WABS×APEC) and subtracted the background described in § 3.1. We obtain a temperature of $13.6^{+13.2}_{-5.1}$ keV and a bolometric luminosity of $L_{\text{bol}} = (10.2 \pm 2.9) \times 10^{44}$ ergs s^{-1} . The measured temperature is far above what we would expect from the luminosity. Figure 5 shows the luminosity-temperature relation for a sample of 115 galaxy clusters (Maughan et al. 2008), along with the luminosity and temperature derived for A689 from our values above (pink square). As the Maughan et al. (2008) sample of clusters covers a wide redshift range, the luminosities of the clusters were corrected for the expected self-similar evolution, given by $L_X \times E(z)^{-1}$, where:

$$E(z) = \Omega_{\text{M}0}(1+z)^3 + (1 - \Omega_{\text{M}0} - \Omega_{\Lambda})(1+z)^2 + \Omega_{\Lambda}. \quad (1)$$

The same correction was also applied to the A689 data for the plot. Our luminosity was derived within the same annular region as the cluster temperature and extrapolated both inward and outward in radius between $(0-1)r_{500}$ (where r_{500} represents the radius at which the density of the cluster is 500 times the critical density of the Universe at that redshift) using parameters from a β -profile fit to the surface brightness profile. This takes into account our exclusion of

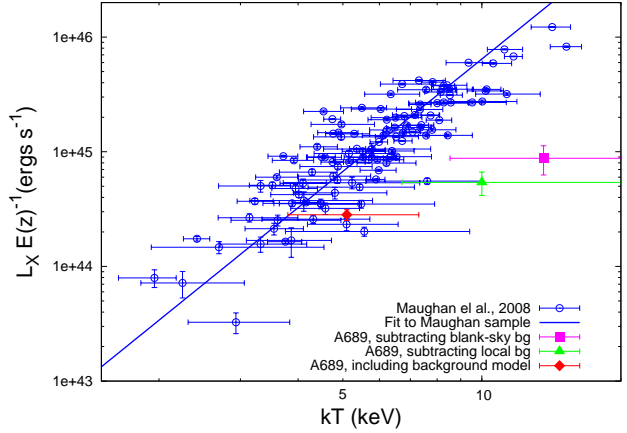


Figure 5. Luminosity-Temperature relation of a sample of 115 clusters of Maughan et al. (2008) (blue open circles). The luminosities are measured within $[0 < r < 1]r_{500}$ and the temperatures within $[0.15 < r < 1.0]r_{500}$, in order to minimize the effect of cool cores on the derived cluster temperature. Our derived temperatures for A689 are overplotted for comparison (pink square, green triangle, red diamond) (see § 3.2).

the region near the central point source within the cluster, and the extrapolation to r_{500} is in order to compare with the Maughan et al. (2008) sample. Our r_{500} value was determined from the temperature and using the relation between r_{500} and T given in Vikhlinin et al. (2006).

The high temperature for A689 could be an indication that our observation suffers from background flaring which would lead to an overestimate of the cluster temperature. However, no evidence is found that the spectrum of the blank-sky background differs from that of the local background (Figure 4), or that the background of the observation suffers from periods of flaring (Figure 1). To investigate the sensitivity of the temperature to our choice of background, we repeated the analysis using a local background region far from the cluster emission (see Fig 2). We obtained a temperature of $10.0^{+13.8}_{-3.3}$ keV. This temperature is again anomalous given the luminosity-temperature relation (Fig 5, green triangle). The luminosity is derived using the same method as above, only this time using this new value for the temperature to derive r_{500} . The spectrum with a local background subtracted is shown in Figure 6. We see an excess of photons in the $\sim 6-9$ keV band, which might have an effect on the spectral fit. We perform the same fit using a local background, however this time fitting in the 0.6–6.0 keV band to ignore these excess high energy photons. We obtain a temperature of $9.4^{+8.7}_{-2.9}$ keV.

Figure 5 shows that the temperature is high for the luminosity, or the cluster is X-ray under-luminous. Before considering a physical interpretation for the apparently high cluster temperature, we investigated possible systematic effects from the background subtraction. This was done by independently modeling the background.

We model the background based upon a physical representation of its components. Our model consists of a thermal plasma APEC model, two power-law components and five Gaussian components. The APEC model and one of the

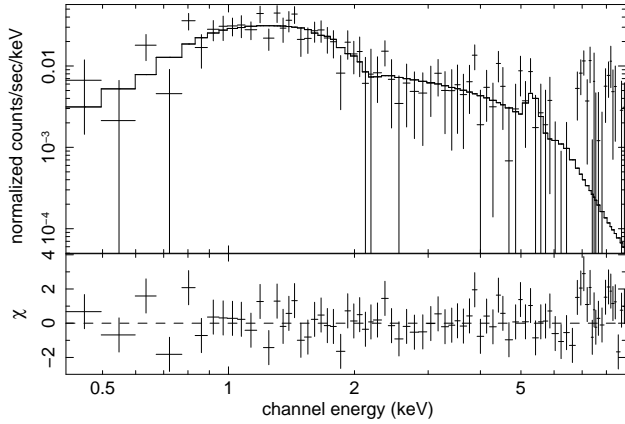


Figure 6. Spectrum of the cluster with the local background subtracted fitted with an absorbed thermal plasma model, with a reduced statistic of $\chi^2_\nu=1.45$ ($\nu=79$).

power-law components are convolved with files describing the telescope and instrument response (the Auxiliary Response File (ARF) and Redistribution Matrix File (RMF)), and are intended to model soft X-ray thermal emission from the Galaxy and unresolved X-ray background. The second power-law component is not convolved with the ARF as it is used to describe the high energy particle background, which does not vary with effective area. The five Gaussian components are similarly not convolved, as these are used to model line features in the spectrum caused by the fluorescence of material in the telescope and focal plane caused by high energy particles.

As described below and summarized in Table 2, the parameters of this background model were fit to the blank-sky background, local background or high energy cluster regions or taken from the literature, in order to build the most reliable model possible. We start by modeling blank-sky background in the region we used to extract our cluster spectrum, with the model outlined above. This allows us to place reasonable constraints on the line energy and widths of each Gaussian component, and the slope of the unconvolved power-law. We find line features at energies of 1.48, 1.75, 2.16, 7.48 and 8.29 keV. We also model the convolved power-law component, fixing the slope at a value of 1.48 taken from Hickox & Markevitch (2006). The normalisation of this power-law component will then be used throughout our modeling process, scaled by area where necessary. A spectrum of the blank-sky background and a fit using our model are shown in Figure 7.

Next we further constrained model parameters by fitting our high-energy Gaussian and unconvolved power-law components in the 5.0-9.0 keV band within the cluster region. At these energies, the emission is dominated by particle background. We fix the line energies and widths to those found in the blank-sky background and fit for the normalisations. This fit finds a slope of the power-law consistent with that found in the blank-sky background. We therefore fix the slope of the power-law at $\Gamma=0.0061$, as found for the blank-sky background, and fit for the normalisation. We finally fit the low energy Gaussians and APEC normalisation model parameters in a local background region far from the cluster emission. The high energy Gaussians and uncon-

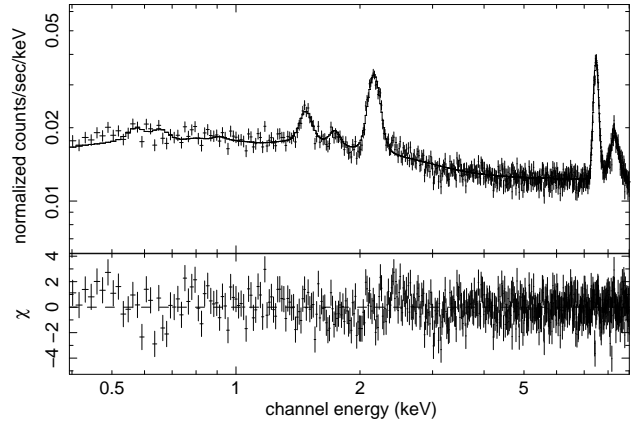


Figure 7. Spectrum of the blank-sky background in the source region and corresponding the fit (see Sect. 3.2), $\chi^2_\nu=1.17$ ($\nu=585$).

convolved power-law components are frozen at the values found in the blank-sky and cluster regions, with the normalisations scaled by area. The convolved power-law component is frozen at the values found in the blank-sky background and the normalisation is scaled by area. The Gaussian features at 1.48, 1.75 and 2.16 keV are frozen at the energies and widths found in the blank-sky background. The temperature of the APEC model is frozen at 0.177 keV (taken from Hickox & Markevitch 2006). We note that our APEC temperature is not well constrained by our data, but this is a weak component. A spectrum of the local background and the corresponding fit with the model are shown in Figure 8.

We now model the cluster with an absorbed thermal plasma (WABS×APEC) model, including the background model outlined above. The normalisations of the background APEC component and the Gaussians at energies 1.48, 1.75 and 2.16 keV were scaled by the ratio of the areas from the local background region to the cluster region. The normalisations of the fluorescent lines also vary with detector position. To account for this effect in the low energy (<3 keV) lines (where we must fit the normalisations in the off-axis local background region), we measure the relative change in the normalisations of each line between the local background and source regions in the blank-sky background data. The normalisation of each low energy Gaussian component in the fit to the cluster data is scaled for the different detector of the cluster region by the relative change in normalisation determined above (in addition to the geometrical scaling for size of the extraction region). The unconvolved power-law and Gaussians at 7.48 and 8.29 keV are all frozen at the values found in the 5.0-9.0 keV cluster region fit. The normalisation of the convolved power-law is frozen at the value found in the blank-sky background. All parameters of the model used to describe the background are frozen in the corresponding cluster fit, we also freeze the redshift at 0.279 and the abundance at 0.3. Our fit yields a temperature of $5.1^{+2.2}_{-1.3}$ keV ($\chi^2_\nu=1.15$ ($\nu=79$)). We measure a bolometric luminosity of $L_{\text{bol}} = 1.7 \times 10^{44}$ erg s⁻¹. The result is shown in Figure 5 (red diamond). The spectrum with the corresponding fit to the cluster including the background model is shown in Figure 9.

Component	Represents	Parameter	Value	Where measured
Convolved power-law	Unresolved X-ray bg	slope	1.48	Hickox & Markevitch (2006)
		normalisation	4.11×10^{-6}	blank-sky bg
Unconvolved power-law	Particle bg	slope	0.061	blank-sky bg
		normalisation	0.015	5.0-9.0 keV cluster region
Gaussian 1	Al K α fluorescence	energy	1.48 keV	blank-sky bg
		width	0.022 keV	blank-sky bg
		normalisation	1.82×10^{-4}	local bg
Gaussian 2	Si K α fluorescence	energy	1.75 keV	blank-sky bg
		width	0.95 keV	blank-sky bg
		normalisation	1.45×10^{-2}	local bg
Gaussian 3	Au M $\alpha\beta$ fluorescence	energy	2.16 keV	blank-sky bg
		width	0.045 keV	blank-sky bg
		normalisation	2.24×10^{-3}	local bg
Gaussian 4	Ni K α fluorescence	energy	7.48 keV	blank-sky bg
		width	0.022 keV	blank-sky bg
		normalisation	5.73×10^{-3}	5.0-9.0 keV cluster region
Gaussian 5	Cu + Ni fluorescence	energy	8.29 keV	blank-sky bg
		width	0.168 keV	blank-sky bg
		normalisation	4.56×10^{-3}	5.0-9.0 keV cluster region
APEC	Galactic foreground emission	kT	0.177 keV	Hickox & Markevitch (2006)
		abundance	1.0	solar abundance
		redshift	0	Galactic
		normalisation	2.9×10^{-5}	local bg

Table 2. Table of the individual model components used to represent the background, with a brief interpretation of each component, individual component parameters, parameter values and where each value is calculated. All normalisations are measured in photons/keV/cm²/s at 1 keV, and scaled to the cluster region. Blank-sky background parameters were derived in the same region and the local background were measured in an area 2.45 times that of the cluster and therefore the normalisations reduced by this factor. The low energy Gaussians were also corrected due to the normalisation dependence with position on the detector (see text).

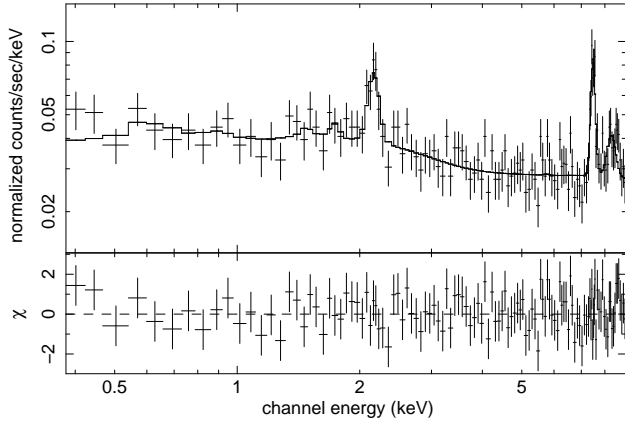


Figure 8. Spectrum of the local background and corresponding fit (see Sect 3.2). $\chi^2_\nu = 0.79$ ($\nu = 120$).

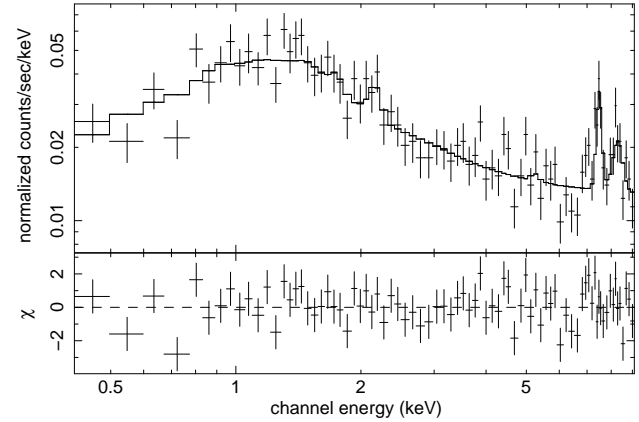


Figure 9. Spectrum of the cluster plus background fit with an absorbed thermal plasma model including a background model (see Sect 3.2). $\chi^2_\nu = 1.15$ ($\nu = 79$).

4 THE CENTRAL POINT SOURCE

The point source is displayed in Figure 10. The presence of strong readout streaks indicate that the point source is likely to be affected by pile-up. The readout streaks occur as X-rays from the source are received during the ACIS parallel frame transfer, which provides 40 μ s exposure per frame in each pixel along the streak. We detail our analysis of the point source and estimate of the pileup fraction in the following section.

4.1 X-ray Analysis of the Point Source

As a first test of the predicted pile-up, we compared the image of the point source to the *Chandra* Point Spread Function (PSF). We made use of CIAO tool MKPSF to create an image of the on-axis PSF following the method outlined in Donato et al. (2003). This consists of merging 7 different monochromatic PSFs chosen and weighted on the basis of the source energy spectrum between 0.3 and 8 keV. This method can be summarized as follows:

- (i) We first extract the energy distributions of the pho-

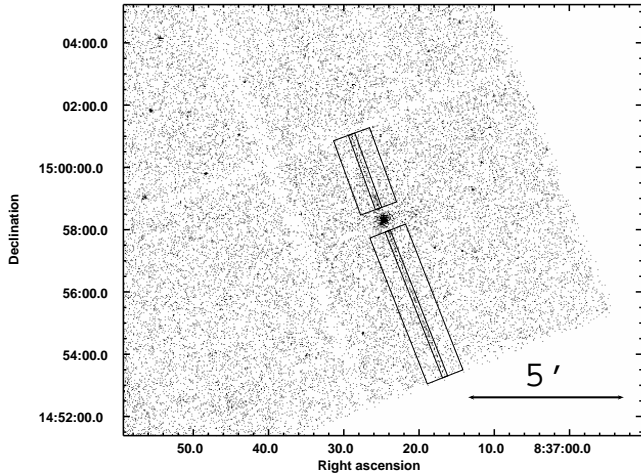


Figure 10. *Chandra* image of A689 showing the regions used for extracting spectra of the readout streak (inner rectangles) and the corresponding background regions for the readout streak (outer rectangles).

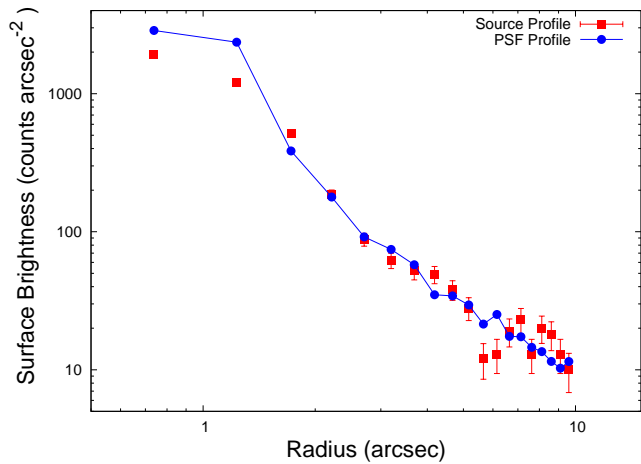


Figure 11. Surface brightness profiles of the point source (red squares) and the composite PSF (blue circles) in the 0.3-8.0 keV band, normalised to agree in the 2.46-4.92 arcsec radii region.

tons from a circular region centered on the peak brightness of the source with a radii of 2.5".

(ii) We choose seven discrete energy values at which to creating each PSF, with the number of counts at each energy corresponding to that PSF's 'weight'.

(iii) Using MKPSF we create seven monochromatic PSFs at the position of the point source on the detector and co-added them. Each PSF is weighted by its relative normalisation (found in the previous step).

Once we obtained the composite PSF, we normalised it to the counts within an annulus (inner and outer radius 2.46 and 4.92 arcsec respectively) in order to avoid any effects of pile-up in the central region. We then compare surface brightness profiles of the point source and PSF to look for evidence of pile-up in the core of the point source image. Figure 11 shows the radial surface brightness profiles of the point source (red) and the composite PSF (blue). We find that the point source and PSF agree well in the wings of the

PSF ($> 2.46''$) and that there is an excess in the PSF surface brightness above that of the point source at the peak of the source. This is consistent with the flattening of the source profile relative to that of the PSF due to pileup in the core. The PSF then gives an estimate of the non piled up count rate. Given this count rate we use PIMMS⁴ to estimate a pile-up fraction of 65%.

We also compute a second estimate of the core count rate using the ACIS readout streak. By fitting a model to the spectrum extracted from the readout streak we can compare this to a spectrum extracted in the core and fitted using a pileup model. We follow the method outlined in Marshall et al. (2005) in order to correct the exposure time of the readout streak spectrum. For an observation of live time t_{live} , a section of the readout streak that is θ_s arcsec long accumulates an exposure time of $t_s = 4 \times 10^{-5} t_{live} \theta_s / (t_f \theta_x)$ s, where $\theta_x = 0.492''$ is the angular size of an ACIS pixel. For our observation, $t_{live} = 13.862$ ks and the frame time parameter $t_f = 3.1$ s, giving $t_s = 165$ s in a streak segment that is $454''$ long. Figure 10 shows the regions used for extracting spectra of the readout and an adjacent background region. This choice of background region ensures the cluster emission is subtracted from the readout streak spectrum. Using the SHERPA package (Refsdal et al. 2009) we fitted an absorbed 1-D power-law model (WABS×POWER-LAW) to the extracted spectrum of the readout streak. We obtain fit parameters for the photon index = $2.33^{+0.34}_{-0.30}$ and a normalisation of 0.0033 ± 0.0005 photons $\text{keV}^{-1} \text{cm}^{-2} \text{s}^{-1}$ ($\chi^2_\nu = 0.34$ ($\nu=63$)). We then extract a spectrum of the point source in a region of radius $5''$, and subtracted the same background as for the readout streak. We once again fitted an absorbed power-law model, including this time a pileup model (jdpileup). We obtain fit parameters for the photon index = $2.22^{+0.05}_{-0.04}$, consistent to that found from the readout streak, and a normalisation of 0.0015 ± 0.0001 photons $\text{keV}^{-1} \text{cm}^{-2} \text{s}^{-1}$ ($\chi^2_\nu = 1.6$ ($\nu=119$)). The extracted spectrum and corresponding fit is shown in Figure 12. The pileup fraction is estimated to be 60%, which is consistent with that found using the PSF count rate. The normalisation found in the fit can be converted to an X-ray flux density for this source, $f_{1 \text{ keV}} = 0.99 \pm 0.07 \mu\text{Jy}$.

4.2 Optical Observations

Abell 689 was observed with the Hubble Space Telescope (HST) with the F606W filter (\tilde{V} -band) on January 20, 2008. Marking the position of the peak X-ray emission of the point source on the HST image, we find that this corresponds to an object resembling an active nucleus in a relatively bright galaxy (Fig 13). We searched the SDSS DR7 archive for information on the spectral properties of this object. At the coordinates of the X-ray point source (SDSS coordinates of $\alpha, \delta = 08^h 37^m 24.7, 14^\circ 58' 19''.8$) we find a blue object with a corresponding relatively featureless spectrum (Fig 14). From SDSS we quote an r-band magnitude of 17.18. The spectrum resembles that of a BL Lac object, a type of AGN orientated such that the relativistic jet is closely aligned to the line of sight. From the H and K lines in the spectrum (dotted green lines in Fig 14), thought to be from the host galaxy,

⁴ <http://cxc.harvard.edu/toolkit/pimms.jsp>

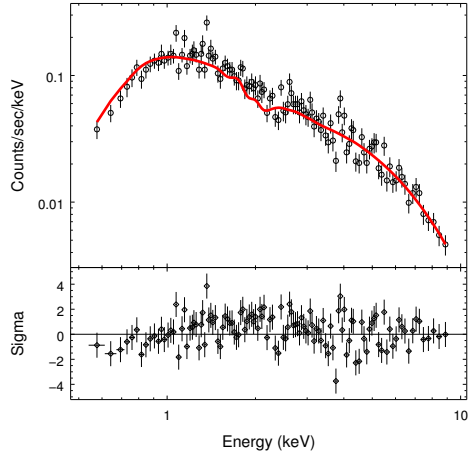


Figure 12. Spectra of the point source fitted with an absorbed power-law, including a pileup model. $\chi^2_\nu=1.6$ ($\nu=119$).

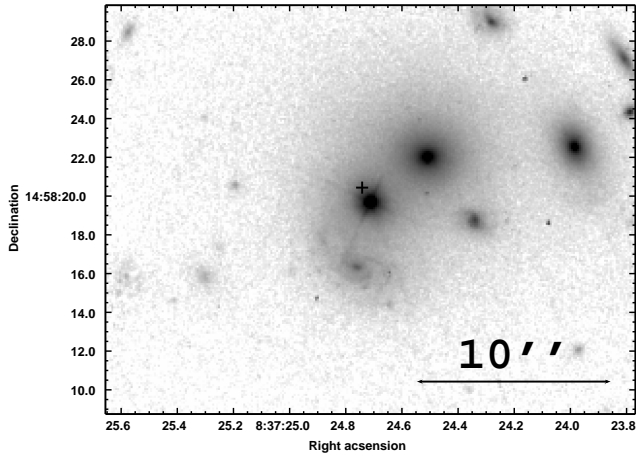


Figure 13. HST image of the point source with a cross marking the position of the peak of the X-ray emission.

the redshift is determined to be $z=0.279$, consistent with the redshift assigned to the cluster (Collins et al. 1995). Using the HST observation we measure an optical flux for the BL Lac of $f_{5997\text{\AA}}=112\text{mJy}$.

4.3 Radio Observations

Archival radio observations of Abell 689 are available, allowing us to determine the radio spectral index, α . We obtained 8.46 GHz data taken in March 1998 from the VLA archive which we mapped using AIPS. The source is unresolved at 8.46 GHz, and we measure a flux density of 18.6 ± 0.27 mJy. We also obtained a 1.4 GHz radio image from the FIRST survey, from which we measure a flux of 62.7 ± 0.25 mJy. From these data we obtain a spectral index of $\alpha_r \sim 0.67 \pm 0.01$. We note that a slight angular extension in the FIRST survey suggests that the 8.46 GHz image may be missing some flux density.

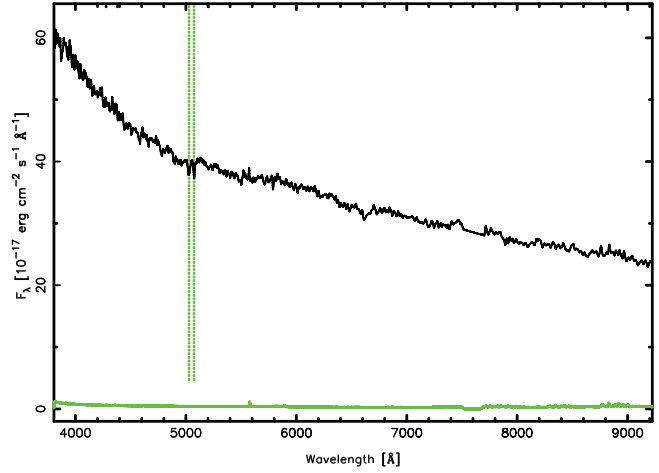


Figure 14. Spectra of the BL Lac from SDSS (SDSS J083724.71+145819.8). The vertical green lines represent the H and K lines thought to be from the host galaxy and the green line at the bottom represents the error spectrum.

5 DISCUSSION

5.1 The ICM properties of Abell 689

We have derived the ICM properties of A689 using three methods of background subtraction. Table 3 shows the spectral properties of the ICM for each of the background treatments we employ with our favored method coming from a physically motivated model of the background components. Through detailed modeling of the local and blank-sky backgrounds for A689, and including this background model in a spectral fit to the cluster, we have determined a temperature and luminosity for A689 of $T = 5.1^{+2.2}_{-1.3}$ keV and $L_{\text{bol}} = 3.3 \times 10^{44}$ erg s $^{-1}$. Plotting these values on the luminosity-temperature plot (Fig 5) and comparing to the large X-ray sample of Maughan et al. (2008), we find that A689 is observed to be at the edge of the observed scatter in the luminosity-temperature relation. This suggests that either the temperature of the ICM has been enhanced or suppression of the luminosity has occurred.

It has been shown that systems that host a radio source are likely to have higher temperatures at a given luminosity. Croston et al. (2005) showed that this is the case for radio-loud galaxy groups, and Magliocchetti & Brüggén (2007) showed that for clusters that host a radio source there is a departure from the typical luminosity-temperature relation, particularly in the case of low mass systems. Croston et al. (2005) also showed, through analysis of *Chandra* and *XMM-Newton* observations, evidence for radio-source interaction with the surrounding gas for many of the radio-loud groups. A similar process could be occurring within A689, which has a confirmed radio source at the center of the cluster. We note that more detailed X-ray and radio observations would be needed in order to test any interaction between the BL Lac and ICM.

The other possible explanation for the offset of radio-loud systems from the luminosity-temperature relation is the suppression of the luminosity, which could be caused by displacement of large amounts of gas due to the interaction of the radio source with the ICM. The interaction

Background Subtraction	r_{500} (arcsec)	T_X (keV)	$L_{X,bol}$ ($\times 10^{44}$ erg s $^{-1}$)	reduced χ^2	degrees of freedom
Blank-sky	1130	$13.6^{+13.2}_{-5.1}$	10.1 ± 2.9	1.19	74
Local	696	$10.0^{+13.8}_{-3.3}$	6.2 ± 1.4	1.45	79
Physically motivated model [†]	266	$5.1^{+2.2}_{-1.3}$	3.3 ± 0.3	1.15	79

Table 3. Table listing the derived spectral properties of A689 for each of the background treatments we employ in our analysis. [†] indicates our favored method for determining the cluster properties of A689.

of the radio source with the ICM will cause an increase in the entropy of the local ICM. This higher entropy gas will be displaced so that it is in entropy equilibrium with the surrounding gas. However, Magliocchetti & Brüggen (2007) showed that there is a correlation between the radio luminosity and the heat input required to produce the observed temperature increment in clusters hosting radio sources. They note that this correlation favors an enhanced temperature scenario caused by the radio galaxy induced heating.

5.2 Comparison with the BCS

A689 was noted in the BCS as having a significant fraction of its flux coming from embedded point sources. We have confirmed that A689 contains a point source at the center of the cluster and is that of a BL Lac object. We stated that the measured X-ray luminosity for A689 as quoted in the BCS ($L_{0.1-2.4\text{keV}} = 3 \times 10^{45}$ erg s $^{-1}$, see § 1), is the third brightest in the BCS. From our follow up observation with Chandra we calculate the luminosity and compare with the BCS value. The luminosities in the BCS are calculated within a standard radius of 1.43 Mpc, which at the redshift of A689 corresponds to a radius of $338''$. We therefore employ the same method as in Sect 3.2 and integrate under a beta model fitted to the derived surface brightness profile and extrapolate inward and outward from $26-206''$ to $0-338''$. The unabsorbed flux in the 0.1 - 2.4 keV band (observed frame) was $f_{0.1-2.4,\text{keV}} = 5.8 \times 10^{-13}$ erg s $^{-1}$ cm $^{-2}$. After k-correction the X-ray luminosity in the 0.1 - 2.4 keV band (rest frame) was $L_{0.1-2.4,\text{keV}} = 2.8 \times 10^{44}$ erg s $^{-1}$. Note that we assume an H_0 of 50 for consistency with the BCS catalog. This value is ~ 10 times lower than that quoted in the BCS, and A689 is now ranked 110th out of 201 in luminosity.

5.3 Classifying the BL Lac

BL Lac objects may be split into ‘High-energy peak BL Lacs’ (HBL) and ‘Low-energy peak BL Lacs’ (LBL), for objects which emit most of their synchrotron power at high (UV-soft-X-ray) or low (far-IR, near-IR) frequencies respectively (Padovani & Giommi 1995). HBL and LBL objects have radio-to-X-ray spectral indices of $\alpha_{rx} \leq 0.75$ and $\alpha_{rx} \geq 0.75$, respectively. We calculate a radio-to-X-ray spectral index for the BL Lac in A689 of $\alpha_{rx} = 0.58 \pm 0.04$. From this value we classify our BL Lac as an HBL type. We also compared our BL Lac with those of Fossati et al. (1998), who investigated the properties of large samples of BL lacs at radio to γ -ray wavelengths. Our value of $\alpha_{rx} = 0.58$ falls into the region $0.35 \leq \alpha_{rx} \leq 0.7$, dominated by X-ray selected BL

Lacs (XBL). This is consistent with the X-ray selection of this cluster. Using the measured HST flux, we also calculate $\alpha_{ro} = 0.50$ and $\alpha_{ox} = 0.77$. These values are not atypical for BL Lac objects (Figure 7 in Worrall et al. 1999).

Donato et al. (2003) tried to determine whether HBLs and LBLs were characterized by different environments. They found that of 5 sources exhibiting diffuse X-ray emission that 4 were HBLs and 1 was an LBL. The BL Lac in A689 continues this trend, as it appears to be an HBL embedded within a cluster environment.

5.4 Evidence for Inverse-Compton Emission

Our initial analysis of the extended emission in A689 yielded temperature estimates that were significantly higher than expected based upon its X-ray luminosity. We also found evidence for an hard excess of X-ray photons in the 6.0-9.0 keV band of the cluster spectrum. Before assigning a physical cause we must be careful to eliminate systematic effects in the background subtraction, as underestimating the particle background will give a hard excess. This is unlikely to be the case here as a high temperature was obtained when either a blank-sky and local background was used.

When using our background model instead of subtracting a background spectrum, the cluster temperature was more consistent with its luminosity (Fig 5). This appears to be due to the unconvolved power law fitting a hard excess in the cluster region. In order to assess what impact the high-energy particle component has on the cluster temperature, we varied the normalisation of the unconvolved power-law component of our background model (sect. 3.2) within its 1σ errors. The temperature ranged from 3.86 to 8.51 keV. Thus small changes in the particle background have a significant influence on the cluster temperature. Our power-law component was derived within the cluster region in the 5.0-9.0 keV band, so our background model may be removing a physical hard X-ray component associated with the cluster. We assess the possible properties of such a component by re-deriving the normalisation of the unconvolved power-law component in the local background region, scaling this value by the ratio of the areas, and using this value for the unconvolved power-law normalisation in the background model for our cluster fit. We find a power-law normalisation of 0.0129 photons keV $^{-1}$ cm $^{-2}$ s $^{-1}$ (as opposed to 0.0149 photons keV $^{-1}$ cm $^{-2}$ s $^{-1}$ in the cluster region). Using this value and re-fitting (Fig 15), we find a cluster temperature of $14.3^{+15.6}_{-5.4}$ keV. This suggests that the hard component is spatially associated with the cluster.

Bonamente et al. (2007) find a similar excess of X-ray emission in the cluster A3112, which is known to have a central AGN. It is argued that this excess may be due to

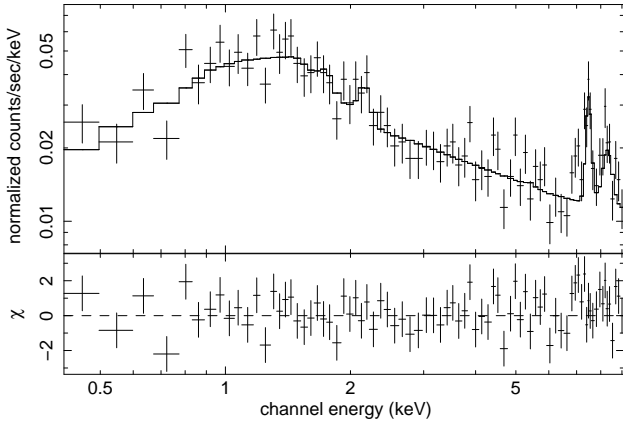


Figure 15. Spectrum of the cluster including our physically motivated model, with the normalisation of the unconvolved power-law component derived in the local background region. $\chi^2_{\nu}=1.17$ ($\nu=79$)

emission of a non-thermal component. Relativistic electrons in the intergalactic medium will cause CMB photons to scatter into the X-ray band (inverse Compton scattering). The same process could occur in A689, with the relativistic particles responsible for the inverse Compton scattering provided by the jets of the BL Lac.

In order to test the assumption of inverse-Compton emission, we add a convolved power-law component with $\alpha=1.5$ (appropriate for modeling IC emission from aged electrons). We fit for the normalisation of this added power-law component and freeze all other parameters of the background and cluster model. We note that we use the normalisation of the unconvolved power-law found in the local background region as found above (a value of 0.0129). When fit, the χ^2 increases slightly but the fit is still acceptable at the 95% confidence level. From the additional power-law component we measure a 1 keV flux density of ~ 7 nJy. If the X-ray emission is from scattering of the CMB by an aged population of electrons of power-law number index 4.0, we can determine what the implied synchrotron emission would be at 1.4 GHz, given plausible magnetic fields. Clusters typically have magnetic fields of a few μG (Carilli & Taylor 2002). The NVSS survey would have detected a flux density of ~ 10 mJy over the entire cluster. Adopting a 1.4 GHz flux density limit of 10 mJy, we require a magnetic field of $B \leq 2 \mu\text{G}$ over the cluster to avoid over-predicting radio emission. We also calculate a value for the minimum-energy magnetic field, $B_{\text{E_min}}$, that would give a 1.4 GHz flux density of $S_{1.4 \text{ GHz}} = 10$ mJy, which in this case is $B_{\text{E_min}} = 7.5 \mu\text{G}$. For a flux density of $S_{1.4 \text{ GHz}} = 5$ mJy, we would require a magnetic field of $1.6 \mu\text{G}$ and $B_{\text{E_min}} = 6.5 \mu\text{G}$. Note that $B \propto S_{1.4 \text{ GHz}}^{1/(1+\alpha)}$ and $B_{\text{E_min}} \propto S_{1.4 \text{ GHz}}^{1/(3+\alpha)}$. We conclude that the excess X-ray emission can be attributed to inverse-Compton scattering without over-predicting the radio emission if the magnetic field strength is in a range typical of clusters and within a factor of a few of the minimum energy value.

6 CONCLUSIONS

We have used a 14 ks *Chandra* observation of the galaxy cluster A689 in order to determine the nature of the cluster's point source contamination and to analyze the cluster properties excluding the central point source. Our main conclusions are as follows.

1. Using background subtraction of both local and blank-sky backgrounds, we obtain temperatures which are high relative to the luminosity-temperature relation.
2. We construct a physically motivated model for the background and include this model in a fit to the cluster spectrum. If the particle background in the cluster is allowed to exceed that in the local and blank-sky backgrounds we obtain a temperature of $5.1^{+2.2}_{-1.3}$ keV. However, there is no reason for there to be a higher particle rate in the specific region of the CCD in which the cluster lies. A hard excess needed to bring the temperature to a reasonable value must have a different origin.
3. We confirm the presence of a point source within A689 as suspected in the BCS. When excluding the point source and using our derive background model we find a luminosity of $L_{0.1-2.4 \text{ keV}} = 2.8 \times 10^{44} \text{ erg s}^{-1}$, a value ~ 10 times lower than quoted in the BCS.
4. From the X-ray analysis of the point source we find a “flat-topped” point source with a pileup fraction of $\simeq 60\%$.
5. Optical observations of the cluster from SDSS and HST lead us to conclude that the point source is a BL Lac type AGN.
6. We classify the BL Lac as an ‘High-energy peak BL Lac’ with $\alpha_{rx}=0.58 \pm 0.04$.
7. We interpret the hard X-ray excess needed to bring the cluster temperature to a reasonable value as inverse-Compton emission from aged electrons that may have been transported into the cluster from the BL Lac.

We have shown here not only the importance of resolving and excluding point sources in cluster observations, but also the effect these point sources can have when determining the ICM properties of galaxy clusters. The detailed analysis we have performed here may not however be suitable for all clusters as it is unclear whether this analysis can be performed at higher redshifts. Separating the point source and cluster emissions becomes increasingly difficult at high redshifts, however *Chandra* has proved capable at resolving point source emission in clusters to $z \sim 2$ (e.g. Andreon et al. 2009). Resolving point source and cluster emission out to high redshift becomes more important with redshift due to the evolution of the number density of point sources within clusters (Galametz et al. 2009). The area used to model the background components associated with the high energy cluster regions will decrease spatially with redshift, and separating the between thermal and inverse Compton emissions at higher redshift will become increasingly difficult (Fabian et al. 2003), due to the increase in the energy density of the CMB with redshift.

ACKNOWLEDGMENTS

We thank J.Price for useful discussions regarding the SDSS and Hubble data. We thank Ewan O’Sullivan and Dominique Sluse for useful discussions on the nature of the

point source. We thank the anonymous referee for valuable comments and suggestions. PG also acknowledges support from the UK Science and Technology Facilities Council.

REFERENCES

- Abell, G. O. 1958, *ApJS*, 3, 211
- Allen S. W., Schmidt R. W., Ebeling H., Fabian A. C., van Speybroeck L., 2004, *MNRAS*, 353, 457
- Andreon, S., Maughan, B., Trinchieri, G., & Kurk, J. 2009, *A&A*, 507, 147
- Bonamente, M., Nevalainen, J., & Lieu, R. 2007, *ApJ*, 668, 796
- Carilli, C. L., & Taylor, G. B. 2002, *ARA&A*, 40, 319
- Collins C. A., Guzzo L., Nichol R. C., Lumsden S. L., 1995, *MNRAS*, 274, 1071
- Croston, J. H., Hardcastle, M. J., & Birkinshaw, M. 2005, *MNRAS*, 357, 279
- Dahle H., Kaiser N., Irgens R. J., Lilje P. B., Maddox S. J., 2002, *ApJS*, 139, 313
- Del Popolo A., Costa V., Lanzafame G., 2010, *A&A*, 514, A80+
- Donato D., Gliozzi M., Sambruna R. M., Pesce J. E., 2003, *A&A*, 407, 503
- Ebeling H., Edge A. C., Allen S. W., Crawford C. S., Fabian A. C., Huchra J. P., 2000, *MNRAS*, 318, 333
- Ebeling H., Edge A. C., Bohringer H., Allen S. W., Crawford C. S., Fabian A. C., Voges W., Huchra J. P., 1998, *MNRAS*, 301, 881
- Fabian, A. C., Sanders, J. S., Crawford, C. S., & Etti, S. 2003, *MNRAS*, 341, 729
- Fossati, G., Maraschi, L., Celotti, A., Comastri, A., & Ghisellini, G. 1998, *MNRAS*, 299, 433
- Galamez, A., et al. 2009, *ApJ*, 694, 1309
- Gioia I. M., Maccacaro T., Schild R. E., Wolter A., Stocke J. T., Morris S. L., Henry J. P., 1990, *ApJS*, 72, 567
- Hickox, R. C., & Markevitch, M. 2006, *ApJ*, 645, 95
- Magliocchetti, M., & Brüggén, M. 2007, *MNRAS*, 379, 260
- Markevitch M., Bautz M. W., Biller B., Butt Y., Edgar R., Gaetz T., Garmire G., Grant C. E., Green P., Juda M., Plucinsky P. P., Schwartz D., Smith R., Vikhlinin A., Virani S., Wargelin B. J., Wolk S., 2003, *ApJ*, 583, 70
- Marshall, H. L., et al. 2005, *ApJS*, 156, 13
- Maughan, B. J., Jones, C., Forman, W., & Van Speybroeck, L. 2008, *ApJS*, 174, 117
- Padovani, P., & Giommi, P. 1995, *MNRAS*, 277, 1477
- Refsdal B. L., Doe S. M., Nguyen D. T., Siemiginowska A. L., Bonaventura N. R., Burke D., Evans I. N., Evans J. D., Fruscione A., Galle E. C., Houck J. C., Karovska M., Lee N. P., Nowak M. A., 2009, in Varoquaux G., van der Walt S., Millman J., eds, *Proceedings of the 8th Python in Science Conference Sherpa: 1d/2d modeling and fitting in python*. Pasadena, CA USA, pp 51 – 57
- Smith R. K., Brickhouse N. S., Liedahl D. A., Raymond J. C., 2001, *ApJ*, 556, L91
- Vikhlinin A., Kravtsov A., Forman W., Jones C., Markevitch M., Murray S. S., Van Speybroeck L., 2006, *ApJ*, 640, 691
- Vikhlinin A., Voevodkin A., Mullis C. R., van Speybroeck L., Quintana H., McNamara B. R., Gioia I., Hornstrup A., Henry J. P., Forman W. R., Jones C., 2003, *ApJ*, 590, 15
- Voges W., 1992, Technical report, The ROSAT all-sky X ray survey
- Worrall, D. M., Birkinshaw, M., Remillard, R. A., Prestwich, A., Tucker, W. H., & Tananbaum, H. 1999, *ApJ*, 516, 163

This paper has been typeset from a \LaTeX file prepared by the author.